Numerical solution of the inverse source problem for the Helmholtz Equation with multiple frequency data

Gang Bao, Junshan Lin, and Faouzi Triki

Abstract. The inverse source problem of the Helmholtz Equation with multiple frequency data is investigated. Three cases are considered: (1) both the magnitude and phase of measurements on the whole boundary (full aperture data) are available; (2) only limited aperture measurements of the field are available; (3) only the magnitude information of the fields on the boundary is available. A continuation method is introduced which can successfully capture both the macro structures and the small scales of the source function. Numerical examples are presented to demonstrate the efficiency of the method.

1. Introduction

Consider the inverse source problem of determining an unknown scalar source to the homogeneous Helmholtz equation. Motivation for the study of this problem is provided by medical imaging as well as antenna synthesis. In medical application it is desired to use the measurement of the radiated field on the surface of the human brain to infer the abnormalities inside the brain, which produced the measured field [**1, 5, 15, 16**]. In antenna synthesis, the problem is to find the current distribution along a linear antenna which produces the desired radiated field [**4, 13**].

From the point view of mathematical modeling, we make the simplification that the background medium in which the source is imbedded is homogeneous. We also restrict our discussion to the two dimensional case. For a homogenous background medium, the generalization to the three dimensional case is straightforward. Assume that the source function $S(x)$ is compactly supported with support volume $\tau \subset \Omega \subset \mathbb{R}^2$, where Ω is a bounded domain with smooth boundary Γ. Moreover, we assume that $\text{dist}(\tau, \Gamma) := \min\{|x - y|;\ x \in \tau,\ y \in \Gamma\} > 0$. Then the radiating field u generated by the source S satisfies the following Helmholtz equation with the Sommerfield radiation condition:

$$\begin{cases} \Delta u + k^2 u = S & \text{in } \mathbb{R}^2, \\ \dfrac{\partial u}{\partial r} - iku = o(r^{-1/2}) & \text{as } r \to \infty. \end{cases} \tag{1.1}$$

2010 *Mathematics Subject Classification.* 35R30, 35Q60, 65N21.

Key words and phrases. Inverse source problem, Helmholtz equation, multiple frequency.

The first two authors were supported in part by the NSF grants DMS-0908325, CCF-0830161, EAR-0724527, DMS-0968360 and the ONR grant N000140210365.

Here $r = |x|$, k is the wavenumber of the radiating field. If $S \in L^2(\tau)$, the forward problem of finding u for a given source S is well-posed. Moreover, by Green's formula and the radiation condition, the solution to (1.1) is given by

$$u(x) = \int_\tau \Phi(k|x-y|)S(y)dy\ , \tag{1.2}$$

where $\Phi(k|x-y|) = -\frac{i}{4}H_0^1(k|x-y|)$ is the fundamental solution for the Helmholtz equation in $\mathbb{R}^2$. The function H_0^1 denotes the Hankel function of the first kind of order zero.

Having defined the forward problem, we are ready to discuss the inverse source problem (ISP). We first begin with the single frequency case. Let ν denote the unit outward normal to the boundary Γ. For the inverse problem, it is assumed that both the radiated field u_k and its normal derivative $\frac{\partial u_k}{\partial \nu}$ are measured on Γ for some fixed k. The subscript k is introduced here to denote the radiated field with fixed wavenumber k, i.e. u_k is the solution to (1.1) with wavenumber k. From data $\{u_k, \frac{\partial u_k}{\partial \nu}\}$ we want to reconstruct the corresponding unknown source function $S(x)$, which produces the measured field pattern on Γ.

More precisely, for fixed wavenumber k, we define the radiation operators $L_k^{(1)}$, $L_k^{(2)}$ from $L^2(\tau) \to \text{Ł}^2(\Gamma)$ as

$$L_k^{(1)}(S)(x) = \int_\tau \Phi(k|x-y|)S(y)dy \quad \text{for } x \in \Gamma, \tag{1.3}$$

$$L_k^{(2)}(S)(x) = \int_\tau \frac{\partial \Phi(k|x-y|)}{\partial \nu(x)} S(y)dy \quad \text{for } x \in \Gamma. \tag{1.4}$$

The inverse source problem is to find $S(x) \in L^2(\tau)$ such that the following linear equations are satisfied simultaneously

$$L_k^{(1)}(S)(x) = u_k(x), \quad L_k^{(2)}(S)(x) = \frac{\partial u_k}{\partial \nu}(x) \quad \text{for } x \in \Gamma. \tag{1.5}$$

It should be pointed out that the inverse problem with single frequency data is not well-posed:

(1) The solution to (1.5) is not unique, i.e., the source function can not be uniquely determined from the measurement on the surface Γ. This is due to the existence of the non-radiating source, whose radiating field vanishes identically outside the support volume τ [**11, 20**].
(2) The problem is severely ill-posed for low wavenumbers, that is, an infinitesimal noise in the measurement will give rise to large errors in the reconstruction solution. In fact, it can be shown that the singular values of forward maps $L_k^{(1)}$ and $L_k^{(2)}$ decay exponentially for low k [**10**] , as shown in Figure 1, where we plot the first 120 singular values of $L_k^{(1)}$ and $L_k^{(2)}$ for $k = 1$. Thus, for the fixed frequency inverse problem (1.5), the best stability estimate would be the logarithm stability.

In this paper, instead of dealing with the single frequency inverse problem, we propose to use multiple frequency data to reconstruct the source function. More precisely, we assume that measurements on the boundary are available for a range

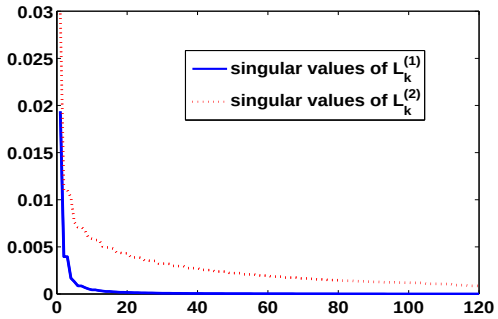

FIGURE 1. The first 120 singular values of $L_k^{(1)}$ and $L_k^{(2)}$ when $k = 1$.

of wavenumbers $[k_{min}, k_{max}]$, that is, we have data $\{u_k, \frac{\partial u_k}{\partial \nu}\}$ available on Γ with k ranges from k_{min} to k_{max}. As before, here u_k is the solution to (1.1) with fixed wavenumber k, k_{min} denotes the lowest wavenumber and k_{max} is the largest wavenumber. The inverse problem with multifrequency data may be formulated as follows:

$$\textit{Find } S \in L^2(\tau) \textit{ such that for all } k \in [k_{min}, k_{max}],$$
$$L_k^{(1)}(S)(x) = u_k(x),\ L_k^{(2)}(S)(x) = \frac{\partial u_k}{\partial \nu}(x) \quad \forall x \in \Gamma.$$

The present numerical study of the inverse problem is motivated by our recent uniqueness and stabilty results [**10**]. In fact, we have proved that with the multi-frequency data available, the inverse problem attains a unique solution. Moreover, under suitable regularity assumptions on S, the stability increases with higher k_{max}, and the Hölder type stability estimate can be obtained if k_{max} is sufficiently large compared to the size of the τ [**10**]. In fact, both theoretical results and numerical evidences on related works also suggest that higher wavenumber information may yield increased stability. In [**17**], Isakov proved the increased stability for Schrödinger potential from DtN map with higher wavenumber. Recent works on the closely related inverse medium scattering problem also confirm this phenomenon [**6, 7, 8, 9, 12**].

Although this inverse problem is linear, and each operator $L_k^{(1)}$ ($L_k^{(2)}$ respectively) is independent for different k, solving the problem directly by a simple assembling of all operators together to a whole one $L = [L_{k_{min}}^{(1)}, L_{k_{min}}^{(2)}, \cdots, L_{k_{max}}^{(1)}, L_{k_{max}}^{(2)}]^T$ would require a tremendous amount of computer memory, which exceeds the limit of computing resources even for supercomputers. In addition, each $L_k^{(1)}$ or $L_k^{(2)}$ involves a dense matrix when discretized. Thus the discretization of the entire operator L would be a large dense matrix.

Instead of solving the whole problem directly, in this paper, we introduce a continuation scheme to reconstruct the source $S(x)$. Roughly speaking, we march along the wavenumber from the lowest wavenumber k_{min} to the highest wavenumber k_{max}. With an initial guess $S(x) = S_0(x)$ at $k = k_{min}$, sequentially we update the solution at a higher wavenumber, where at each fixed wavenumber k, the Landweber

iteration is applied as a regularization scheme. Heuristically, such kinds of continuation methods are based on the uncertainty principle. It is well known that for an optical microscope, $\lambda/2$ is the highest resolution that one can expect, where λ is the wavelength. This is the so called diffraction limit. In fact, the multi-frequency measurements on Γ with $k_{min} \leq k \leq k_{max}$ is equivalent to the Fourier modes of the source $S(x)$ in the aperture $B_{k_{min}}^{k_{max}} := \{ \xi \in \mathbb{R}^2 \ : \ k_{min} \leq |\xi| \leq k_{max} \}$. By the continuation method starting from the lowest wavenumber, it is expected that the small Fourier modes of the source $S(x)$ could be recovered at comparably small k (or large wavelength λ). With increasing wavenumbers, small structures of the source, or the large Fourier modes, can also be captured.

This continuation scheme also applies to the reconstruction for the limited aperture case, when measurements are available only on part of the boundary. The limited aperture measurement happens, for instance, in medical imaging, where data can only be obtained on the surface of human brain.

Another goal of this paper is to propose a continuation reconstruction method for the case when only the magnitude of measurements is available on the boundary. The problem becomes nonlinear if we do not have the phase information of measurements. Hence, linearization is needed when dealing with the minimization problem at each wavenumber. Our recursive scheme can still reconstruct the source at reasonable accuracy.

It is worth mentioning that M. Eller and N. Valdivia also consider the ISP with multiple frequency [**14**]. However, their numerical approach based on the explicit expressions of the eigenfunctions for the Laplacian is completely different from our method. In particular, our method can deal with general geometries. On the other hand, if the measurements are collected very far away from the support of the source, the inverse source problem maybe reduced to an inversion of a spherical Radon transform. Such kind of transform has been studied in the context of photoacoustic imaging recently by H. Ammari and his collaborators [**2**]. In case of small inhomogeneities, we refer the reader to [**3**] as well as the references therein. It should be pointed out that our method only assumes that the source function is of compact support. No size assumption is needed for the source support.

The rest of the paper is outlined as follows. In Section 2, we introduce the continuation method, details of the implementation are discussed. In Section 3, several numerical examples are shown to illustrate the efficiency and stability of the method. Both full aperture and limited aperture cases are considered. Section 4 is concerned with the case when the phase information of measurements on the boundary is unknown. Concluding remarks are presented in Section 5.

2. Continuation method to reconstruct the source function

As discussed in the previous section, the multi-frequency measurements on Γ with $k_{min} \leq k \leq k_{max}$ contain the information of the Fourier modes of the source $S(x)$ in the aperture $B_{k_{min}}^{k_{max}} := \{ \xi \in \mathbb{R}^2 \ : \ k_{min} \leq |\xi| \leq k_{max} \}$. This can be seen from the following derivation. In fact, by Green's formula and noting that $e^{-ix\cdot\xi}$ satisfies the homogeneous Helmholtz equation with $k = |\xi|$, then

$$\hat{S}(\xi) = \frac{1}{2\pi} \int_\Omega (\Delta u_k + k^2 u_k) e^{-ix\cdot\xi} dx = \frac{1}{2\pi} \int_\Gamma \left(\frac{\partial u_k}{\partial \nu} + i(\xi \cdot \nu) u_k \right) e^{-ix\cdot\xi} ds.$$

This holds for all $\xi \in B_{k_{min}}^{k_{max}}$ with $|\xi| = k$. The Fourier transform $\hat{S}(\xi)$ of the source $S(x)$ is defined by $\hat{S}(\xi) = \frac{1}{2\pi} \int_{\mathbb{R}^2} S(x) e^{-ix\cdot\xi}$ dx. Therefore, the field pattern with low frequency on Γ contains the macro structure information of the source, while the high frequency field pattern contains the micro information of the source.

In the reconstruction, we first capture the macro structure of the source at the lower wavenumbers (large wavelength). Then, by sequentially increasing the wavenumber, we keep updating the solution until the entire features of the source are successfully reconstructed. The process is described as follows.

Assume that at $k = k_m$, the source function has been recovered with $S = S_m$. Then at a higher wavenumber $k = k_{m+1} := k_m + \delta k_m$, where $\delta k_m > 0$ is the increment, the Landweber iteration is applied to solve (1.5) with $k = k_{m+1}$. The Landweber iteration can be interpreted as the steepest descent algorithm, which is known to be a regularization scheme for linear ill-posed problems. For the convergence property of the scheme, we refer to [**19**].

To be more specific, for $k = k_{m+1}$, define two corresponding minimization problems for (1.5)

$$\min_{S\in L^2(\tau)} \left\| L_k^{(1)}(S) - u_k \right\|_{L^2(\Gamma)} \quad \text{and} \quad \min_{S\in L^2(\tau)} \left\| L_k^{(2)}(S) - \frac{\partial u_k}{\partial \nu} \right\|_{L^2(\Gamma)}.$$

Initially let $S_{m+1} = S_m$, then the steepest descent directions are chosen for these two minimization problems respectively:

$$d^{(1)} = -\Re\left(L_k^{(1)^*} (L_k^{(1)} S_{m+1} - u_k) \right), \tag{2.1}$$

$$d^{(2)} = -\Re\left(L_k^{(2)^*} (L_k^{(2)} S_{m+1} - \frac{\partial u_k}{\partial \nu}) \right). \tag{2.2}$$

where $L_k^{(1)^*}$ and $L_k^{(2)^*}$, which are defined from $\L^2(\Gamma) \to L^2(\tau)$, are the adjoint operators of $L_k^{(1)}$ and $L_k^{(2)}$, respectively, and $\Re$ denotes the real part of a function. In other words,

$$\int_\Gamma L^{(1)}(S)\bar{v} ds = \int_\tau S\overline{L_k^{(1)^*}(v)} dx, \ \int_\Gamma L^{(2)}(S)\bar{v} ds = \int_\tau S\overline{L_k^{(2)^*}(v)} dx \quad \forall v \in L^2(\Gamma).$$

With the steepest descent directions defined above, the Landweber iteration updates the solution along these directions by setting:

$$S_{m+1} \longleftarrow S_{m+1} + \alpha d^{(1)}, \quad S_{m+1} \longleftarrow S_{m+1} + \alpha d^{(2)}. \tag{2.3}$$

Here α is the step length. This downhill process is done iteratively until S_{m+1} reaches the admissible accuracy.

The continuation method which marches along the wavenumber from the lowest k_{min} to the highest k_{max} can be summarized as follows:

(1) (*Initialization*)
Let $k_0 = k_{min}$, the lowest wavenumber. Initially set $S_0 = 0$.
(2) (*March along the wavenumber*)
For $m = 0, 1, 2\cdots$, let $k_{m+1} = k_m + \delta k_m$, with δk_m as the increment of the wavenumber. If $k_{m+1} > k_{max}$, where k_{max} is the highest wavenumber, then the marching process stops.

(3) (*Update the solution at $k = k_{m+1}$ by Landweber iteration*)
Set $S_{m+1} = S_m$ as the starting point for the Landweber iteration.
(3.1) For $n = 1, 2, 3, \cdots, N$, choose the steepest descent directions

$$d_n^{(1)} = -\Re\left((L_{k_{m+1}}^{(1)})^*(L_{k_{m+1}}^{(1)} S_{m+1} - u_k)\right),$$

update the solution by $S_{m+1} \longleftarrow S_{m+1} + \alpha_n d_n^{(1)}$.
(3.2) For $n = 1, 2, 3, \cdots, N$, choose the steepest descent directions

$$d_n^{(2)} = -\Re\left((L_{k_{m+1}}^{(2)})^*(L_{k_{m+1}}^{(2)} S_{m+1} - \frac{\partial u_k}{\partial \nu})\right),$$

update the solution by $S_{m+1} \longleftarrow S_{m+1} + \alpha_n d_n^{(2)}$.
Go to (2) for the next higher wavenumber.

For the reconstruction with data available on the aperture $\tilde{\Gamma}$ only (limited aperture measurement), where $\tilde{\Gamma}$ is a subset of the boundary Γ, $L_k^{(i)}$ and $(L_k^{(i)})^*$ are replaced by $L_{k,\tilde{\Gamma}}^{(i)}$ and $(L_{k,\tilde{\Gamma}}^{(i)})^*$ respectively in the continuation method ($i = 1, 2$). Here $L_{k,\tilde{\Gamma}}^{(i)}$ is the restriction of the radiation operator $L_k^{(i)}$ on $\tilde{\Gamma}$, and $(L_{k,\tilde{\Gamma}}^{(i)})^*$ is the adjoint operator of $L_{k,\tilde{\Gamma}}^{(i)}$.

Next, we discuss some practical implementation issues. The support volume τ is partitioned by a uniform rectangular grid. The size h of the each rectangular grid needs to be chosen carefully. To capture both the amplitude and the phase of the filed pattern correctly when k is large, h needs to be small. We follow one rule of thumb by setting h such that $k_{max}h < 1/2$. More discussion on the choice of h for numerical computation of wave propagation with high wavenumber can be found in [**18**] and the references therein. On this rectangular grids, the operators $L_k^{(1)}$ and $L_k^{(2)}$ are discretized by the trapezoidal quadrature rule, which leads to dense matrices. At each reconstruction, it is time expensive to calculate every discretized $L_k^{(1)}$ and $L_k^{(2)}$ for $k \in [k_{min}, k_{max}]$ in real time. Thus it is desirable to store all these operators on the hard disk first, and import them at each reconstruction when needed.

We set a uniform increment by letting $\delta k_m = \delta k$ for all m. In fact, the increment parameter δk depends on the scale feature of the source function. Theoretically, the smaller δk we choose, the better reconstruction we can get. However, small δk will lead to expensive computation, while too large δk will deteriorate the reconstruction image. We set $\delta k = 0.2$ in our numerical examples.

In the practical implementation, the step length α_n has to be chosen between 0 and $\min(\frac{1}{\left\|L_k^{(1)}\right\|^2}, \frac{1}{\left\|L_k^{(2)}\right\|^2})$ such that the Landweber iteration serves as a regularization scheme [**19**]. In our numerical examples, α_n is set as $1 + k/k_{max}$, that is to make the step length larger as the convergence become slower. For a fixed wavenumber $k = k_{m+1}$, the number of the iterations N can be determined by the discrepancy principle [**19**]. Our numerical experiments indicate that $N = 30$ is sufficient to obtain admissible accuracy.

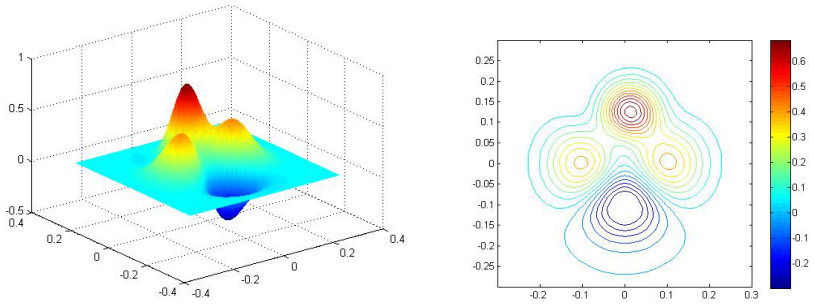

(a) (b)

FIGURE 2. Real source function (a) and its contour plot (b).

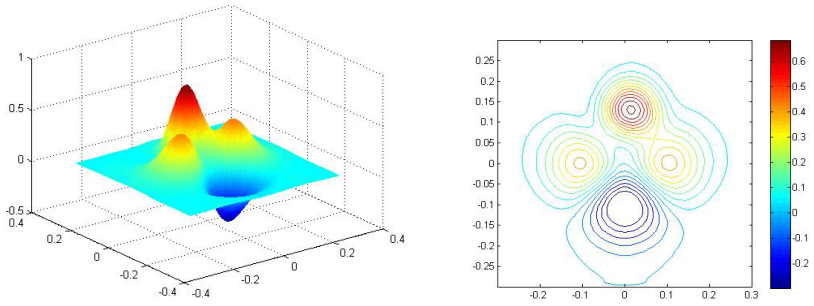

(a) (b)

FIGURE 3. Reconstructed solution (a) and its contour plot (b) at $k_{max} = 61$.

3. Numerical Examples

In this section, several numerical examples are presented to illustrate the efficiency of the continuation method. In all our examples, the support volume of the source function is $\tau = [-0.3, 0.3] \times [-0.3, 0.3]$, which lies in the domain Ω such that $dist(\tau, \Gamma) = 0.05$ (Γ is the boundary of Ω). The measurements $\{u_k, \dfrac{\partial u_k}{\partial \nu}\}$ are collected on Γ for $k \in [k_{min}, k_{max}]$. We set $k_{min} = 1$ in the following numerical examples.

Example 3.1 Assume that the true source

$$S(x_1, x_2) = 1.1e^{-200((x_1-0.01)^2)+(x_2-0.12)^2} - 100(x_2^2 - x_1^2)e^{-90(x_1^2+x_2^2)}.$$

The surface plot of the source is shown in Figure 2(a). Figure 2(b) is the contour plot of $S(x_1, x_2)$. We stop the recursion at $k_{max} = 61$. The final reconstruction image and the corresponding contour plot is shown in Figure 3. It can be seen that the reconstructed solution captures both the macro structures and the small scales of the source. Figure 4 is the evolution of the reconstructed solutions at various

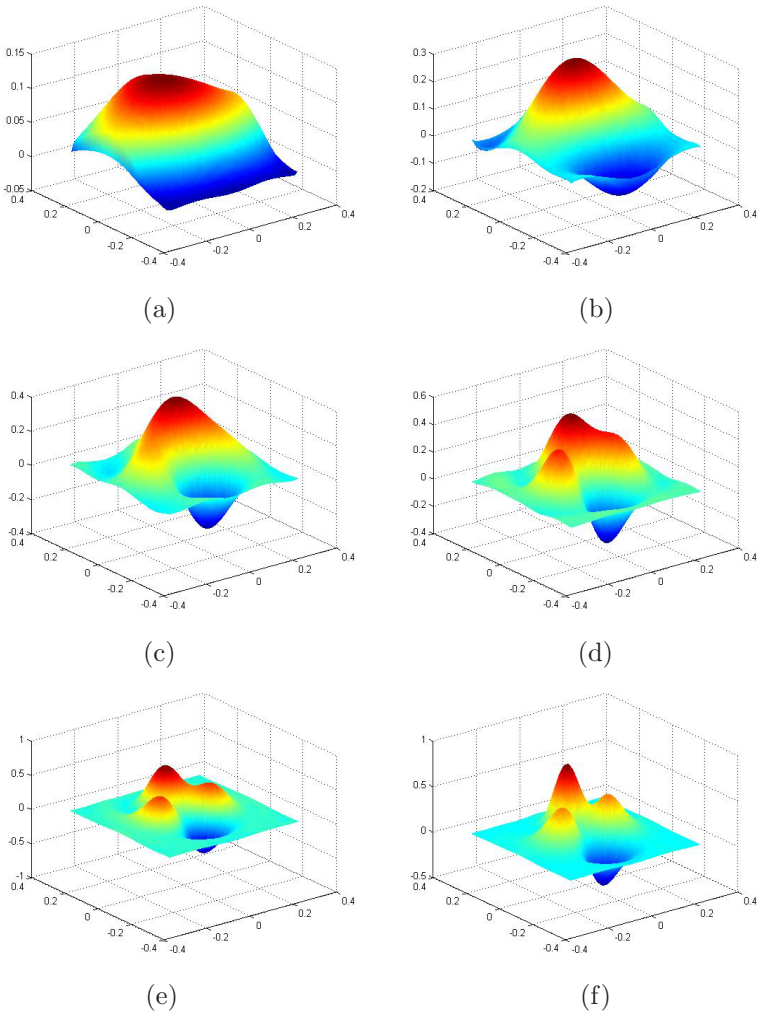

FIGURE 4. Reconstructions at (a) k=9, (b) k=17, (c) k=25, (d) k=33, (e) k=41 and (f) k=61.

wavenumbers. When k is relatively small (with large wavelength), only the main profile of the source can be recovered. However, more and more details are captured as k increases, until the reconstructed solution converges to the real one.

Example 3.2 In this example, the true source consists of two bumps. One is a cone with a circular base, and the other is a cone with an elliptic base. It is defined by

$$S(x_1, x_2) = 0.5[e^{-300((x_1+0.08)^2+(x_2-0.08)^2)} + e^{-300(1.8(x_1-0.1)^2+(x_2+0.1)^2)}].$$

The surface and the image of $S(x_1, x_2)$ are plotted in Figure 5. To test the stability of the method against noise, we add the measurements with 10% uniformly distributed noise. The final reconstruction and the corresponding numerical error

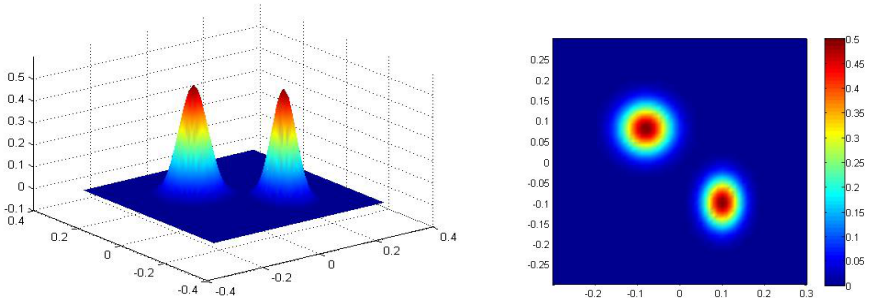

FIGURE 5. Surface plot (Left) and image of the real source function (Right).

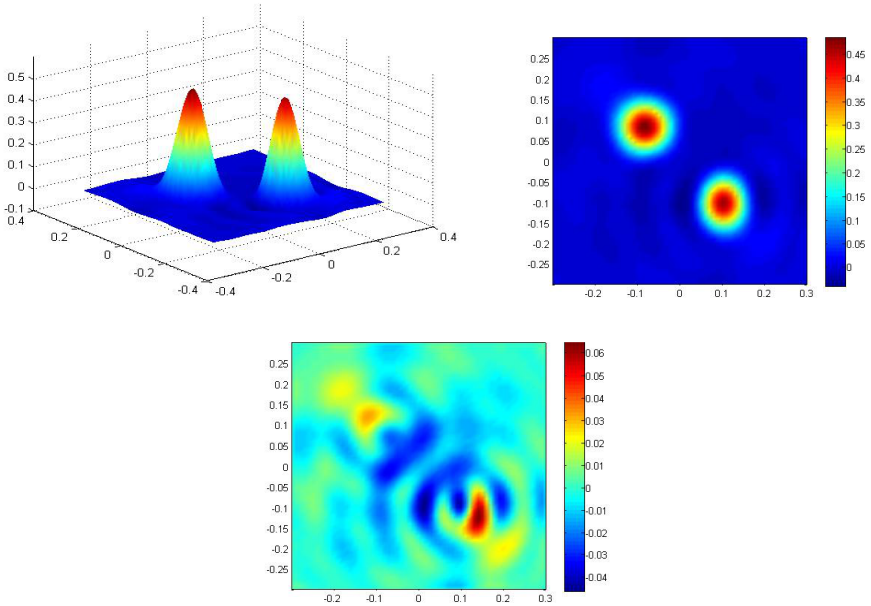

FIGURE 6. Surface plot(Top left) and image (Top right) of reconstructed solution at $k_{max} = 61$ with 10% noise in measurements; the numerical error (Bottom).

at $k_{max} = 61$ are plotted in Figure 6. From the figures we see that not only the two bumps are clearly distinguished, the shape and the magnitude of the source are also recovered.

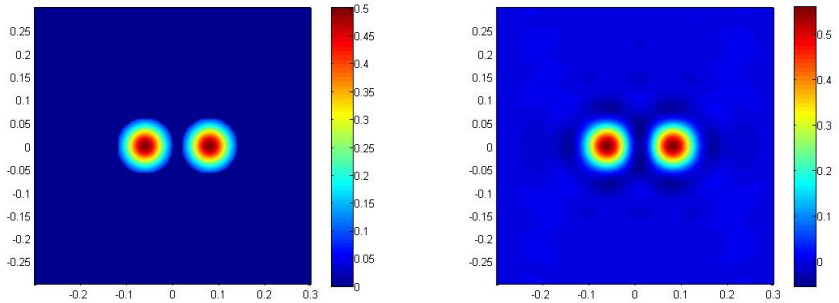

(a) (b)

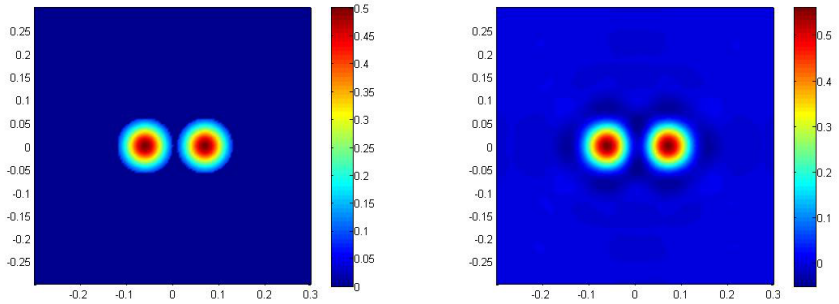

(c) (d)

FIGURE 7. Images of the real source solution (a): d=0.02, (c): d=0.01 and the corresponding reconstructed solutions (b) and (d). 10% noise is added to the measurements. $k_{max} = 79$, wavelength $\lambda \approx 0.08$.

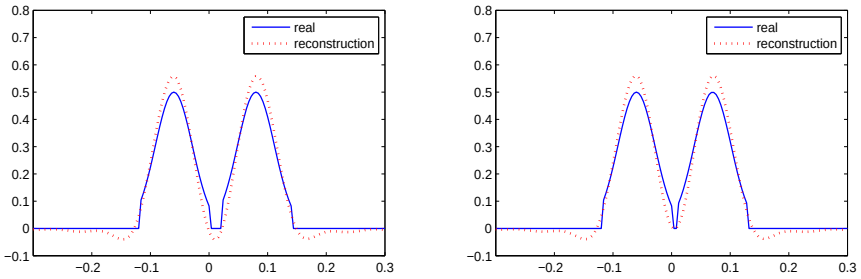

(a) (b)

FIGURE 8. Cross section plot of the real and reconstruction at $x_2 = 0$. 10% noise is added to the measurements. (a): d=0.02, (b): d=0.01. The solid line is the real source, and the dotted line is the numerical one.

Example 3.3 This numerical example demonstrates the resolution of the reconstructed image. The true source function is defined by

$$S(x_1, x_2) = \begin{cases} 0.5\exp(-550r_1^2) & \text{in } B_r(\hat{x}_0, 0); \\ 0.5\exp(-550r_2^2) & \text{in } B_r(\bar{x}_0, 0); \\ 0 \quad \text{elsewhere.} \end{cases}$$

Here $r_1 = \sqrt{(x_1 - \hat{x}_0)^2 + x_2^2}$, $r_2 = \sqrt{(x_1 - \bar{x}_0)^2 + x_2^2}$ and $B_r(x_0, 0)$ represents the disk with radius r centered at $(x_0, 0)$. We set $r = 0.06$ in the numerical experiment. Firstly let $\hat{x}_0 = -0.06$ and $\bar{x}_0 = 0.08$. Therefore, the distance d between two discs is 0.02. The image is plotted in Figure 7(a). We add 10% noise, which is uniformly distributed, to the measurements. In the numerical simulation $k_{max} = 79$, i.e. the smallest wavelength that is used in the simulation is $\lambda \approx 0.08$. Figure 7(b) is the image of the final reconstruction. We also plot the cross section of real and reconstruction at $x_2 = 0$ in Figure 8(a). It can be seen that two discs are clearly distinguished.

Next we make the the distance d between two discs smaller by keeping $\hat{x}_0 = -0.06$ fixed and setting $\bar{x}_0 = 0.07$, thus $d = 0.01$. Figure 7(c) (d) are the corresponding real and reconstructed images. Figure (8)(b) is the cross section plot at $x_2 = 0$. The two discs can still be distinguished in the reconstruction. Thus the subwavelength resolution is achieved by our continuation method. Moreover, the reconstructed image also captures the small details inside two discs, though the discontinuities are smoothed out in the numerical result due to regularization.

Example 3.4 (Limited aperture case) We investigate the reconstruction of the source with limited aperture multi-frequency data in this example. Reconsider Example 3.1 of the mountain shape source function. We consider three cases: (1) $\{u_k, \frac{\partial u_k}{\partial \nu}\}$ are measured on 3/4 of the surface. That is, data are available on three sides of the rectangle $[-0.35, 0.35] \times \{-0.35, 0.35\}$ and $\{0.35\} \times [-0.35, 0.35]$. (2) 1/2 of the surface, measurement are made on $[-0.35, 0.35] \times \{-0.35\}$ and $\{0.35\} \times [-0.35, 0.35]$. (3) 1/4 of the surface with measurement on $[-0.35, 0.35] \times \{-0.35\}$. The final reconstruction images at $k_{max} = 61$ and the corresponding contour plots are shown in Figure 9. The reconstruction can still capture both the main feature and the small structure of the source when the measurement aperture is larger than half of the entire surface, but the image deteriorates with smaller aperture size. It is also evident from the figure that we are no longer able to reconstruct the fine features of the source accurately when the measurement aperture is only 1/4 of the full aperture.

4. Reconstruction with the magnitude of the field pattern

The measured field pattern on the boundary Γ can be represented by

$$u_k(x) = |u_k(x)|e^{i\theta_{k,x}} \quad \text{and} \quad \frac{\partial u_k}{\partial \nu}(x) = |\frac{\partial u_k}{\partial \nu}(x)|e^{i\phi_{k,x}} \quad \text{for } x \in \Gamma.$$

Due to the limitation of the measurement instrument, in practice there are cases when only the magnitude of the field pattern $|u_k|$ and $|\frac{\partial u_k}{\partial \nu}|$ can be obtained, while the phase θ and ϕ are unknown. In this section we investigate the reconstruction of the source from the measured $|u_k|$ and $|\frac{\partial u_k}{\partial \nu}|$ only, but multiple frequency measurement is still assumed.

Define the forward maps $F_k^{(1)}$ and $F_k^{(2)}$ associated with wavenumber k, which map the source function $S(x)$ to the magnitude of the field pattern $|u_k|$ and $|\frac{\partial u_k}{\partial \nu}|$

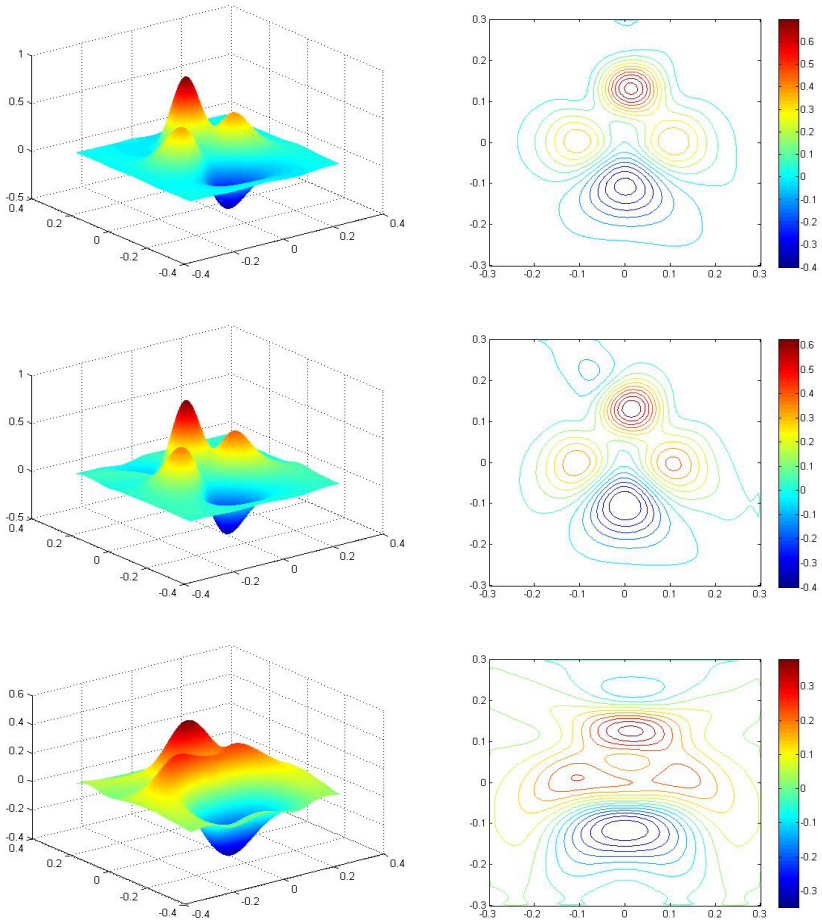

FIGURE 9. Reconstruction image and the contours with data measured on 3/4 of the surface (Top), 1/2 surface (Middle) and 1/4 of the surface (Bottom) .

on Γ respectively:

$$F_k^{(1)}(S) = \sqrt{\left(\Re L_k^{(1)}(S)\right)^2 + \left(\Im L_k^{(1)}(S)\right)^2}, \tag{4.1}$$

$$F_k^{(2)}(S) = \sqrt{\left(\Re L_k^{(2)}(S)\right)^2 + \left(\Im L_k^{(2)}(S)\right)^2}, \tag{4.2}$$

where $L_k^{(1)}$ and $L_k^{(2)}$ are radiation operators defined by (1.3), $\Re$ and $\Im$ are operators that map the function to its real and imaginary part respectively. The Fréchet derivative of $F_k^{(i)}(S)$ is represented by

$$DF_{k,S}^{(i)} = \frac{1}{F_k^{(i)}(S)} \left(\Re L_k^{(i)}(S) \cdot \Re L_k^{(i)} + \Im L_k^{(i)}(S) \cdot \Im L_k^{(i)}\right), \quad i = 1, 2. \tag{4.3}$$

The subscript S is introduced to denote that the Fréchet derivatives are linear operators depending on S for fixed k.

Once again, we employ the continuation method of marching along the wavenumbers to reconstruct the source $S(x)$. Assume that at $k = k_m$, the reconstruction is $S_m(x)$. Then at a higher wavenumber $k = k_{m+1}$, the forward map $F^{(1)}_{k_{m+1}}(S)$ is linearized by

$$F^{(1)}_{k_{m+1}}(S) = F^{(1)}_{k_{m+1}}(S_m) + DF^{(1)}_{k_{m+1},S_m}(S - S_m) + O(\|S - S_m\|_2^2).$$

Note that $F^{(1)}_{k_{m+1}}(S)$ is the measured magnitude $|u_{k_{m+1}}|$ of the field, then $F^{(1)}_{k_{m+1}}(S) - F^{(1)}_{k_{m+1}}(S_m)$ is actually the residual on the boundary Γ, which we denote by $R^{(1)}_{m+1}$. Neglecting the higher order terms and let $\Delta S^{(1)} = S - S_m$, we get the linearized equation

$$DF^{(1)}_{k_{m+1},S_m}\Delta S^{(1)} = R^{(1)}_{m+1}. \tag{4.4}$$

The Landweber regularization method is applied to solve the linearized equation by marching along the steepest descent directions:

$$\Delta S^{(1)}_{n+1} = \Delta S^{(1)}_n - \alpha(DF^{(1)}_{k_{m+1},S_m})^*[DF^{(1)}_{k_{m+1},S_m}\Delta S^{(1)}_n - R^{(1)}_{m+1}],$$
$$n = 0, 1, 2, \cdots, N-1.$$

Here α is the step length, $(DF^{(1)}_{k_{m+1},S_m})^*$ is the adjoint operator of $DF^{(1)}_{k_{m+1},S_m}$, and N is the number of iterations. Therefore, the reconstruction at $k = k_{m+1}$ is updated by setting

$$S_{m+1} = S_m + \Delta S^{(1)}_N. \tag{4.5}$$

The same linearization procedure is applied for $F^{(2)}_{k_{m+1}}(S)$, and the reconstruction is then updated by $S_{m+1} \leftarrow S_{m+1} + \Delta S^{(2)}_N$. $\Delta S^{(2)}_N$ again is computed by the Landweber iteration:

$$\Delta S^{(2)}_{n+1} = \Delta S^{(2)}_n - \alpha(DF^{(2)}_{k_{m+1},S_{m+1}})^*[DF^{(2)}_{k_{m+1},S_{m+1}}\Delta S^{(2)}_n - R^{(2)}_{m+1}],$$
$$n = 0, 1, 2, \cdots, N-1,$$

where $R^{(2)}_{m+1} = F^{(2)}_{k_{m+1}}(S) - F^{(2)}_{k_{m+1}}(S_{m+1})$ is the residual. Note that here $F^{(2)}_{k_{m+1}}$ and $DF^{(2)}_{k_{m+1}}$ are evaluated at S_{m+1}, which is the update represented by (4.5).

We assume that $k_{min} = 0$, then the imaginary parts of u_0 and $\dfrac{\partial u_0}{\partial \nu}$ are both 0. Hence, u_0 and $\dfrac{\partial u_0}{\partial \nu}$ can be measured directly in practice. We solve

$$L^{(1)}_0(S_0) = u_0, \quad L^{(2)}_0(S_0) = \frac{\partial u_0}{\partial \nu}. \tag{4.6}$$

by the Landweber iteration to get the initial guess S_0.

The recursive reconstruction scheme is summarized as follows:

(1) (*Initialization*).
Let $k_0 = 0$, initially solve (4.6) to get S_0.
(2) (*March along the wavenumber*).
For $m = 0, 1, 2\cdots$, let $k_{m+1} = k_m + \delta k_m$. If $k_{m+1} > k_{max}$, then marching process stops.

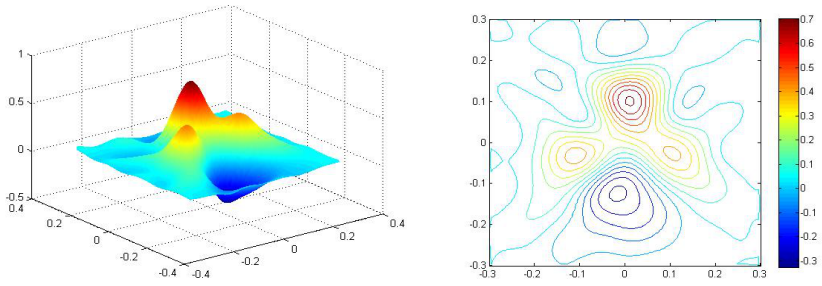

(a) (b)

FIGURE 10. Reconstruction at $k_{max} = 61$ (a) and its contour plot (b).

(3) (*Update the solution at* $k = k_{m+1}$ *by linearization*).
Initially let $S_{m+1} = S_m$.
For $i = 1, 2$:
Set $\Delta S_0 = 0$ as the starting point for the Landweber iteration.
For $n = 0, 1, 2 \cdots N - 1$:
$\Delta S_{n+1} = \Delta S_n - \alpha (DF^{(i)}_{k_{m+1}, S_{m+1}})^* [DF^{(i)}_{k_{m+1}, S_{m+1}} \Delta S_n - R^{(i)}_{m+1}]$.
END
Update the reconstruction by $S_{m+1} \leftarrow S_{m+1} + \Delta S_N$.
END
Go to (2) for the next higher wavenumber.

Several numerical examples are shown in the following to demonstrate the efficiency of the continuation method. Final reconstruction of the mountain shape source function (the same source as that of Example 3.1) at $k_{max} = 61$ is plotted in Fig 10. Although the accuracy is not comparable to that of the Example 3.1 (with phase information), key macro feature and some small details of the source can still be captured. The loss of accuracy is reasonable since the phase information of the measured field pattern is unknown, and the problem become nonlinear.

Consider the source which composes of two discs, as discussed in Example 3.3, we add 10% uniformly distributed noise to the measurements $|u_k|$ and $|\frac{\partial u_k}{\partial \nu}|$. Figure 11 are the images of final reconstructions and numerical errors at $k_{max} = 79$ for $d = 0.02$ and $d = 0.01$, respectively. d again is the distance between discs. We also compare the cross section of real source and reconstruction at $x_2 = 0$ in Figure 12. It can be seen that two discs can still be distinguished, however, the accuracy is deteriorated when compared with Example 3.3.

5. Conclusion

In this paper, we propose a continuation method to reconstruct the source of the Helmholtz equation with multi-frequency measurements. By marching along the wavenumber, the method can sequentially recover the feature of the source from both full and limited aperture boundary measurements, and is stable. This recursive

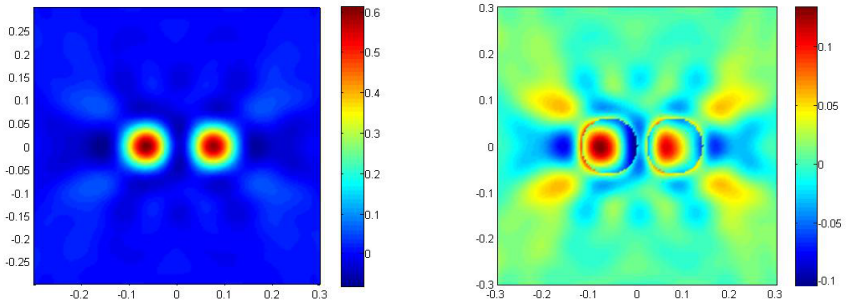

(a) (b)

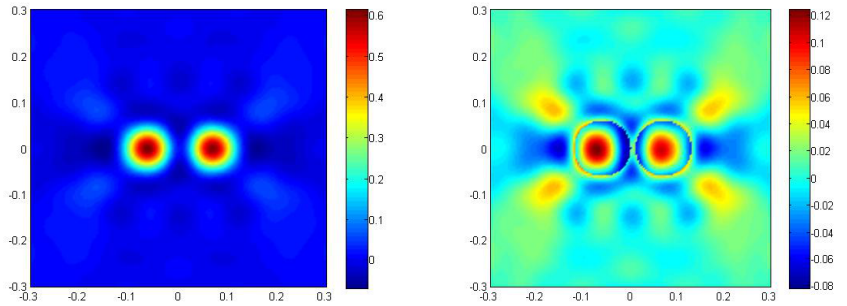

(c) (d)

FIGURE 11. Images of reconstructions with 10% noise in measurements (a): d=0.02, (c): d=0.01. (b) and (d) are the corresponding numerical errors for $k_{max} = 79$, wavelength $\lambda \approx 0.08$.

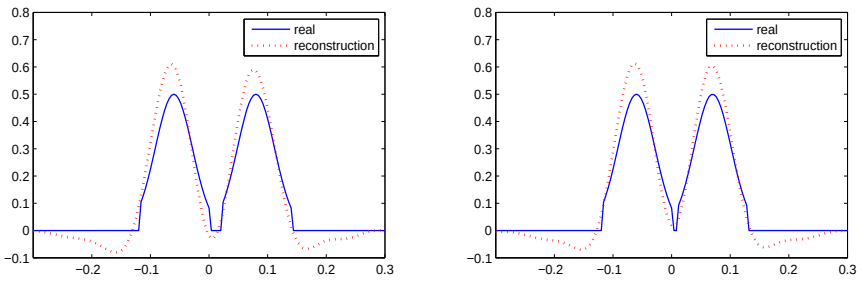

(c) (d)

FIGURE 12. Cross section plot of the real and reconstruction at $x_2 = 0$. 10% noise is added to the measurements. (a): d=0.02, (b): d=0.01. The solid line is the real source, and the dotted line is the numerical one.

scheme can also reconstruct the source successfully when only the magnitude of the field pattern is known. Our ongoing project is to reconstruct the source in

inhomogeneous media, where the wavenumber k depends on the index of refraction of the medium. We will also investigate the ISP for the Maxwell's equations. They have important applications in medical imaging and geophysical inversion.

References

[1] H. Ammari, G. Bao, and J. Fleming, *An inverse source problem for Maxwell's equations in magetoencephalography*, SIAM J. Appl. Math., **62** (2002), 1369-1382.

[2] H. Ammari, E. Bossy, V. Jugnon and H. Kang, *Mathematical modelling in photo-acoustic imaging of small absorbers*, SIAM Review, **52** (2010), 677-695.

[3] H. Ammari and H. Kang, *Reconstruction of Small Inhomogeneities from Boundary Measurements*, Lecture Notes in Mathematics, vol. 1846, Springer-Verlag, Berlin (2004).

[4] T. Angel, A. Kirsch, and R. Kleinmann, *Antenna control and generalized characteristic modes*, Proc. IEEE, **79** (1991), 1559-1568.

[5] R. Albanese and P. Monk, *The inverse source problem for Maxwell's equations*, Inverse Problems, **22** (2006), 1023-1035.

[6] G. Bao and P. Li, *Inverse medium scattering for three-dimensional time harmonic Maxwell equations*, Inverse Problems, **20** (2004), L1-L7.

[7] G. Bao and P. Li, *Inverse medium scattering problems for electromagnetic waves*, SIAM J. Appl. Math., **65** (2005), 2049-2066.

[8] G. Bao and P. Li, *Inverse medium scattering for the Helmholtz equation at fixed frequency*, Inverse Problems, **21** (2005), 1621-1641.

[9] G. Bao and P. Li, *Inverse medium scattering problems in near-field optics*, J. Comput. Math., **25** (2007), 252-265.

[10] G. Bao, J. Lin, and F. Triki, *A multi-frequency inverse source problem*, *J. Diff. Eqn.*, **249** (2010), 3443-3465.

[11] N. Bleistein and J. Cohen, *Nonuniqueness in the inverse source problem in acoustics and electromagnetics*, J. Math. Phys., **18** (1977), 194-201.

[12] Y. Chen, *Inverse Scattering via Heisenberg's Uncertainty Principle*, Inverse Problems, **13** (1997), 1-13.

[13] A. Devaney, E. Marengo, and M. Li, *The inverse source problem in nonhomogeneous background media*, SIAM J. Appl. Math., **67** (2007), 1353-1378.

[14] M. Eller and N. Valdivia, *Acoustic source identification using multiple frequency information*, Inverse Problems, **25** (2009), 115005.

[15] A. Fokas, Y. Kurylev, and V. Marinakis, *The unique determination of neuronal currents in the brain via magnetoencephalogrphy*, Inverse Problmes, **20** (2004), 1067-1082.

[16] S. He and V. Romanov, *Identification of dipole equations*, Wave motion, **28** (1998), 25-44.

[17] V. Isakov, *Increased stability for the Schrödinger potential from the Dirichlet-to-Neumann map*, Discrete Contin. Dynam. Systems, to appear.

[18] F. Ihlennburg and I. Babuska, *Finite element solution of the Helmholtz equation with high wave number (Part I)*, Computers Math. Applic., **30** (1995), No.9, 9-37.

[19] A. Kirsch, *An Introduction to the Mathematical Theory of Inverse Problems*, Applied Mathematical Sciences, vol.120, Springer-Verlag, New York (1996).

[20] E. Marengo and A. Devaney, *Nonradiating sources with connections to the adjoint problem*, Phys, Rev. E, **70** (2004), 037601.

Department of Mathematics, Zhejiang University, Hangzhou 310027, China; Department of Mathematics, Michigan State University, East Lansing, MI 48824, USA

E-mail address: bao@math.msu.edu

Department of Mathematics, Michigan State University, East Lansing, MI 48824, USA

E-mail address: linjunsh@msu.edu

Université Joseph Fourier, L.J.K., 38041 Grenoble Cedex 9, France

E-mail address: Faouzi.Triki@imag.fr